CHALMERS

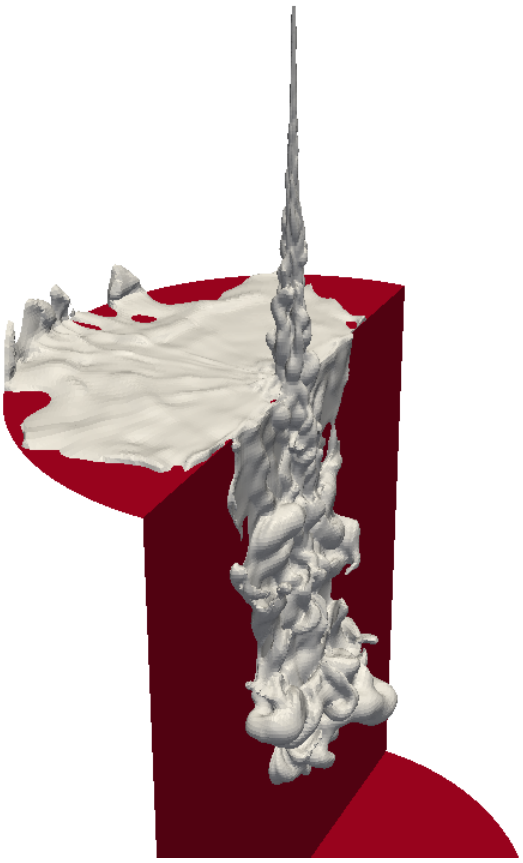

A study of turbulence phenomenas in simplified flow situations of interest for diesel combustion development

Master's Thesis in Solid & Fluid Mechanics

MARTIN HAMMAS
ANDERS RYNELL

Department of Applied Mechanics
Division of Fluid Dynamics
CHALMERS UNIVERSITY OF TECHNOLOGY
Göteborg, Sweden 2011
Master's Thesis 2011:59

MASTER'S THESIS 2011:59

A study of turbulence phenomenas in simplified flow situations of interest for diesel combustion development

Master's Thesis in Solid & Fluid Mechanics

MARTIN HAMMAS
ANDERS RYNELL

Department of Applied Mechanics
Division of Fluid Dynamics
CHALMERS UNIVERSITY OF TECHNOLOGY
Göteborg, Sweden 2011

A study of turbulence phenomenas in simplified flow situations of interest for diesel combustion development

MARTIN HAMMAS
ANDERS RYNELL

Master's Thesis 2011:59
ISSN 1652-8557
Department of Applied Mechanics
Division of Fluid Dynamics
Chalmers University of Technology
SE-412 96 Göteborg
Sweden
Telephone: + 46 (0)31-772 1000

Cover:
Isosurface of $C_{16}H_{34}$ concentration at 6% with the flat plate

Chalmers Reproservice
Göteborg, Sweden 2011

A study of turbulence phenomenas in simplified flow situations of interest for diesel combustion development

Master's Thesis in Solid & Fluid Mechanics
MARTIN HAMMAS
ANDERS RYNELL
Department of Applied Mechanics
Division of Fluid Dynamics
Chalmers University of Technology

Abstract

The interest to investigate real flame propagation in diesel engines lead to this master thesis project where *OpenFOAM* version 1.7.1 (Open Field Operations And Manipulations) has been used to simulate an equivalent high speed diesel jet entering a combustion chamber. In real situations, the fuel enters the domain in liquid phase, then evaporates into a gas. In this work, the jet enters the domain as pure gas phase, i.e. it is treated as if the evaporation occurs instantaneously. When no phase transformation occurs it will be referred to as an equivalent gas jet.

Both standard and tuned versions of the k-ϵ turbulence model have been used in order to validate the similarity of the simulated fuel penetration curves that were compared with the experiments at Chalmers HP/HT combustion chamber and data presented by Siebers and Naber.

After validation of the equivalent gas jet, Large eddy simulations (LES) is used, in order to enhance the level of details in the turbulent gas jet. The main purpose of this project is to be able to analyze the turbulent quantities and structures of the flow, which cannot be done using RANS models. In simulations of transient phenomenas, such as diesel sprays, it is particularly important to get an instantaneous view of the flow field.

The simulation study starts with a simple flow situation and then the complexity gradually increases. Three different geometries have been used. The first one is a free volume, without any interference with the walls and the other two have a flat plate and a curved wall mounted, respectively.

Keywords: CFD, OpenFOAM, LES, jet propagation

Contents

Preface

This Master thesis was carried out at Volvo Technology Corporation (VTEC), department of Energy Conversion during 2011. The main purpose of the project was to simulate a gas jet in a combustion chamber using *OpenFOAM* version 1.7.1 and to further investigate correlations between the turbulence phenomenas created by the jet and the surrounding air. It has been shown that the mixing rate and subsequent combustion is a direct consequence of the shear layer arisen from large velocity gradient cause by the penetrating gas jet. This Master thesis was built on a previous experiment reported by our supervisor Jan Eismark at VTEC [4].

Acknowledgements

First of all we would like to thank our supervisor at VTEC, Jan Eismark for an interesting project. He has been a great support and a source of motivation. Our examiner at Chalmers, professor Lars Davidson, for his guidance throughout the project and experience and knowledge in Large eddy simulation (LES). When major problems arised getting *OpenFOAM* to work at VTEC's computer cluster, Jon-Anders Bäckar was there helping us, assuring progress in our work. Anders Karlsson for his help with sprays, but also in CFD and *OpenFOAM*. Anders Tenstam and Dalibor Cuturic for their help creating meshes in *StarCCM+*. The Swedish Energy Agency and VTEC for the funding of the project (Swedish Energy Agency project number 30754-1).

Göteborg October 2011
Martin Hammas, Anders Rynell

Nomenclature

$\dot{\omega}_k$	Mass rate source term
$\dot{m}_{in}$	Mass flow
ϵ	Dissipation
μ	Dynamic viscosity
ν	Kinematic viscosity
ν_t	Turbulent kinematic viscosity
Φ	Viscous dissipation
ρ	Density
σ_{ij}	Viscous stress tensor
τ_w	Wall shear stress
τ_{ij}	Subgrid-scale viscous stress tensor
C_s	Smagorinsky constant
D_{in}	Inlet side length
g_i	Gravitional acceleration
h	Enthalpy
k	Turbulent kinetic energy
k_{SGS}	SGS turbulent kinetic energy
L	lengthscale
p	Pressure
Pr	Prandtl number
Pr_t	Turbulent Prandtl number
q_i^{SGS}	Subgrid-scale heat flux
R	Specific gas constant
Re	Reynolds number
S_{ij}	Strain-rate tensor
T	Temperature
t	Time
u_*	Friction velocity
u_i	Velocity

V_{ij}	Vorticity tensor
y^+	Dimensionless wall normal unit
Y_k	Specie concentration

1 Introduction

Highly set goals regarding tomorrow's stringent emissions regulations, makes the understanding of todays' diesel engines and all of its processes a prioritized topic of research for engineers around the world. The fuel is injected at high pressure directly into the combustion chamber where it ignites by mixing with hot air produced by isentropic compression. During diesel combustion, the balance between soot formation and oxidation and their history regulate the amount of soot particles present in the exhaust gas. Since the availability of oxidants, especially hydroxyl radicals (OH), is essential for an effective fuel and soot burn-out process, tracking its formation and presence will yield a better understanding of its mixing process. To study the turbulence causing the mixing is therefore essential.

Our objective is to study the turbulence phenomena arising in the combustion chamber due to the injection. Diesel combustion is often modelled using a Eulerian-Lagrangian approach for which a two phase model involving sub-models like evaporation, break-up, droplet collison etc describes the mixing process. In order to focus the study on turbulence, no combustion is considered. The phase transformation is considered to instantaneously occur which means that n-Hexadecane ($C_{16}H_{34}$) is entering the chamber as a gas. An equivalent gas jet is used to verify the similarity and equivalent behavior to a two-phase system, i.e. the gas jet penetration charactersistics should agree with corresponding fuel vapor penetration curves. To obtain the equivalent performance, nozzle area, velocity and the fuel temperature are varied with the constraint of a constant mass flow.

Three different geometries are used to study how the flow field influences the mixing and relevant turbulence properties like the turbulent Reynolds number and vorticity but also pressure, velocity and their gradients, kinetic energy and its magnitude. The first geometry is simply a free volume while the other two have obstacles in shapes of a flat plate and a curved plate.

2 Turbulence theory

2.1 Properties of interest

Some reminder regarding common turbulent vocabulary terms will follow.

2.1.1 Vorticity

Vorticity is a fundamental quantity when studying turbulence. It describes how strong the velocity field is rotating and is given by

$$V_{ij} = \frac{1}{2}\left(\frac{\partial u_i}{\partial x_j} - \frac{\partial u_j}{\partial x_i}\right) \tag{2.1}$$

2.1.2 Wall normal distance y^+

This is a dimensionless number which describes the cell resolution in the wall normal direction. In the near-wall cell, y^+ should be ≤ 1 to assure a physically sound solution. There are corresponding numbers in the other dimensions as well. It is defined as

$$y^+ = \frac{u_* y}{\nu} \tag{2.2}$$

where y is the distance to the nearest wall, ν is the kinematic viscosity and u_* is the friction velocity defined as

$$u_* = \sqrt{\frac{\tau_w}{\rho}} \tag{2.3}$$

where ρ is the density of the fluid and τ_w is the wall shear stress, i.e.

$$\tau_w = \mu\left(\frac{\partial u_1}{\partial x_2}\right)_{x_2=0} \tag{2.4}$$

2.1.3 Turbulent kinetic energy

The higher the turbulent kinetic energy, the more turbulence is present in the flow. If $k = 0$ then the flow is said to be laminar, i.e. there are no turbulent fluctuations. The kinetic energy is defined as

$$k = \frac{1}{2}\overline{u_i' u_i'} \tag{2.5}$$

This is simply the trace of the Reynolds stress tensor, $\overline{u_i' u_j'}$ devided by two.

2.1.4 Reynolds number

The Reynolds number is a dimensionless quantity that describes the flow. Turbulent flow is characterized by high Reynolds number. At low Re number the flow is said to be laminar. The transition between laminar and turbulent flow is characterized by the critical Reynolds number, Re_{crit}.

$$Re = \frac{inertial force}{viscous force} = \frac{\rho U L}{\mu} = \frac{U L}{\nu} \tag{2.6}$$

2.2 Governing equations

The governing equations representing fluid flows are the conservation laws of physics. The fluid is regarded as a continuum which means that the fluid properties are assumed to vary continuously from one point to another. The central axioms then states that the conservation of mass (continuity statement), linear momentum (Newton's second law of motion) and energy (first law of thermodynamics) are fulfilled. When dealing with combustion and compressible flows, the latter is often expressed using enthalpy instead. They are commonly refered to as the Navier Stokes equations and are given below

$$\frac{\partial \rho}{\partial t} + \frac{\partial \rho u_i}{\partial x_i} = 0 \tag{2.7}$$

$$\frac{\partial \rho u_i}{\partial t} + \frac{\partial \rho u_i u_j}{\partial x_j} = -\frac{\partial p}{\partial x_i} + \frac{\partial \sigma_{ij}}{\partial x_j} + \rho g_i \tag{2.8}$$

$$\frac{\partial \rho h}{\partial t} + \frac{\partial \rho u_i h}{\partial x_i} = \frac{\partial p}{\partial t} + u_i \frac{\partial p}{\partial x_i} + \frac{\partial}{\partial x_i}\left[\frac{\mu}{Pr}\frac{\partial h}{\partial x_i}\right] + \Phi \tag{2.9}$$

where x_i (i = 1,2,3) are the cartesian coordinates, u_i are the cartesian components of the velocity, t stands for time, ρ is the density, p is the pressure, σ_{ij} is the viscous stress tensor, g_i represents the gravitational acceleration, h is the enthalpy, μ is the kinematic viscosity and Pr is the Prandtl number. Φ is viscous dissipation which will be neglected. The term σ_{ij} is defined by

$$\sigma_{ij} = \mu\left(2S_{ij} - \frac{2}{3}S_{kk}\delta_{ij}\right) \tag{2.10}$$

where S_{ij} is the strain-rate tensor given by

$$S_{ij} = \frac{1}{2}\left(\frac{\partial u_i}{\partial x_j} + \frac{\partial u_j}{\partial x_i}\right) \tag{2.11}$$

In order to couple the equations, since the number of unknown are greater than the number of equation, the assumption of an ideal gas is used. The problem is that almost all flows of engineering significance are turbulent. Main features regarding turbulence are the random nature of the flow, three dimensional flow characteristics, large Reynolds numbers (inertia forces totally dominates compared to viscous forces), it is dissipative and governed by rotational flow structures, i.e vorticity. To be capable of representing the effects of turbulence, one common way is to decompose the random properties into a mean value and some statistical properties of their fluctuations. When doing so, additional terms, often called the Reynolds stresses appear in the governing equations. Different approaches to solve these equations are available and which one that will be used is always a matter of resolution and computational cost. Considered here are the k-ϵ model as well as LES.

2.3 Favre filtering

A common filtering approach named Favre filtering is used when dealing with compressible flow calculations. By doing so the governing equations are expressed in a convenient form, i.e. a form very similar to that of the unfiltered equations. For instance, if the velocity and density are decomposed into a mean value as well as a fluctuating one, the continity equation (2.7) will look like

$$\frac{\partial \bar{\rho}}{\partial t} + \frac{\partial \bar{\rho}\bar{u}_j}{\partial x_j} + \frac{\partial \overline{\rho' u_j'}}{\partial x_j} = 0 \tag{2.12}$$

An additional term, the last term in (2.12), arises from correlations between the density and velocity fluctuations. This term has to be modelled and other terms will also appear in the momentum and energy equation. By using an averaging procedure, known as Favre averaging, the number of unknown terms can be reduced. Flow properties are decomposed as follows

$$u = \tilde{u} + u'' \tag{2.13}$$

where the filtered part of u is expressed as

$$\tilde{u} = \frac{\overline{\rho u}}{\bar{\rho}} \tag{2.14}$$

The instantaneous property can be written as

$$u = \tilde{u} + u'' = \frac{\overline{\rho u}}{\bar{\rho}} + u'' \tag{2.15}$$

By using this on the convective term and time averaging, also knowing that $\overline{\rho u''}$=0, gives

$$\frac{\partial \bar{\rho}}{\partial t} + \frac{\partial \bar{\rho}\tilde{u}_i}{\partial x_i} = 0 \tag{2.16}$$

As can be seen it has the same form as equation (2.7).

2.4 k-ϵ turbulence model

First of all the instantaneous variables are decomposed into a mean and a fluctuating value, known as Reynolds decomposition. The mean value is obtained through time averaging and as an example, velocity is shown

$$u_i = \bar{u}_i + u_i' \tag{2.17}$$

If all variables are decomposed in this way, inserted into Navier Stokes equations (2.7, 2.8 and 2.9) and then time averaged, the RANS (Reynolds Averaged Navier Stokes) equations are obtained.

$$\frac{\partial \bar{\rho}}{\partial t} + \frac{\partial \bar{\rho}\bar{u}_j}{\partial x_j} = 0 \tag{2.18}$$

$$\frac{\partial \bar{\rho}\bar{u}_i}{\partial t} + \frac{\partial}{\partial x_j}\left(\overline{\rho \bar{u}_i \bar{u}_j} + \overline{\rho u_i' u_j'}\right) = -\frac{\partial \bar{p}}{\partial x_i} + \frac{\partial \bar{\sigma}_{ij}}{\partial x_j} + \bar{\rho}\bar{g}_i \tag{2.19}$$

$$\frac{\partial \bar{\rho}\bar{h}}{\partial t} + \frac{\partial}{\partial x_i}\left(\overline{\rho \bar{u}_i \bar{h}} + \overline{\rho u_i' h'}\right) = \frac{\partial \bar{p}}{\partial t} + u_i \frac{\partial \bar{p}}{\partial x_i} + \frac{\partial}{\partial x_i}\left[\frac{\mu}{Pr}\frac{\partial \bar{h}}{\partial x_i}\right] \tag{2.20}$$

As can be seen, two terms are added to the equations. The term appearing in the momentum equation (2.19) is called the Reynolds stress tensor and has to be modelled since it is unknown. A common way is to use the Boussinesq assumption where an eddy (or turbulent) viscosity is introduced to model the unknown stresses. Also the term $\overline{u_i'h'}$ is modelled using this assumption where an turbulent Prandtl number is used. Clarification is given below

$$\overline{u_i'u_j'} = -\nu_t \left(\frac{\partial \bar{u}_i}{\partial x_j} + \frac{\partial \bar{u}_j}{\partial x_i} \right) + \frac{2}{3}\delta_{ij}k = -2\nu_t \bar{S}_{ij} + \frac{2}{3}\delta_{ij}k \tag{2.21}$$

$$\overline{u_i'h'} = -\frac{\nu_t}{Pr_t}\frac{\partial \bar{h}}{\partial x_i} \tag{2.22}$$

The reason for solving the transport equation for k and ϵ is to be able to express the turbulent viscosity using these two quantities, i.e.

$$\nu_t = C_\mu \frac{k^2}{\epsilon} \tag{2.23}$$

where $C_\mu = 0.09$. Using the Boussinesq assumption for the production term and the standard gradient hypothesis for the diffusion, except for the pressure diffusion, which is negligble, the modelled equation for k is obtained. The modelled equation for ϵ is derived using k-equation as a starting point and they both looks like;

$$\begin{aligned} \frac{\partial \bar{\rho} k}{\partial t} + \frac{\partial \bar{\rho} k \bar{u}_i}{\partial x_i} &= \frac{\partial}{\partial x_i}\left[\left(\mu + \frac{\mu_t}{\sigma_k} \right) \frac{\partial k}{\partial x_i} \right] + \mu_t \left[2\bar{S}_{ij}\bar{S}_{ij} - \frac{2}{3}\left(\frac{\partial \bar{u}_k}{\partial x_k} \right)^2 \right] \\ &- \frac{2}{3}\bar{\rho} k \frac{\partial \bar{u}_i}{\partial x_i} - \bar{\rho}\epsilon \end{aligned} \tag{2.24}$$

$$\begin{aligned} \frac{\partial \bar{\rho} \epsilon}{\partial t} + \frac{\partial \bar{\rho} \epsilon \bar{u}_i}{\partial x_i} &= \frac{\partial}{\partial x_i}\left[\left(\mu + \frac{\mu_t}{\sigma_\epsilon} \right) \frac{\partial \epsilon}{\partial x_i} \right] + \mu_t C_{\epsilon 1} \frac{\epsilon}{k} \left[2\bar{S}_{ij}\bar{S}_{ij} - \frac{2}{3}\left(\frac{\partial \bar{u}_k}{\partial x_k} \right)^2 \right] \\ &- \frac{2}{3} C_{\epsilon 1} \bar{\rho}\epsilon \frac{\partial \bar{u}_i}{\partial x_i} - C_{\epsilon 2}\bar{\rho}\frac{\epsilon^2}{k} + C_{\epsilon 3}\bar{\rho}\epsilon \frac{\partial \bar{u}_i}{\partial x_i} \end{aligned} \tag{2.25}$$

The standard values for the coefficients are given in Table 2.1

Table 2.1: Constants of the standard k-ϵ model

$C_{\epsilon 1}$	$C_{\epsilon 2}$	$C_{\epsilon 3}$	σ_k	σ_ϵ
1.44	1.92	-0.33	1	1.3

2.5 Large Eddy Simulations (LES)

In LES, the variables are filtered (volume averaged) instead of time averaged. This mean that the filtered variables are functions of both space and time. Note that $\tilde{(.)}$ for now on, means a filtered quantity. The filtered Navier-Stokes equations that is solved using LES are

$$\frac{\partial \bar{\rho}}{\partial t} + \frac{\partial \bar{\rho}\tilde{u}_i}{\partial x_i} = 0 \tag{2.26}$$

$$\frac{\partial \bar{\rho}\tilde{u}_i}{\partial t} + \frac{\partial \bar{\rho}\tilde{u}_i\tilde{u}_j}{\partial x_j} = -\frac{\partial \bar{p}}{\partial x_i} + \frac{\partial \bar{\sigma}_{ij}}{\partial x_j} - \frac{\partial \tau_{ij}}{\partial x_j} \tag{2.27}$$

$$\frac{\partial \bar{\rho}\tilde{h}}{\partial t} + \frac{\partial \bar{\rho}\tilde{u}_i\tilde{h}}{\partial x_i} = \frac{\partial \bar{p}}{\partial t} + u_i\frac{\partial \bar{p}}{\partial x_i} + \frac{\partial}{\partial x_i}\left[\frac{\mu}{Pr}\frac{\partial \bar{h}}{\partial x_i} + q_i^{SGS}\right] \tag{2.28}$$

where the Favre-filtered viscous stress tensor,

$$\bar{\sigma}_{ij} = \mu\left(2\tilde{S}_{ij} - \frac{2}{3}\tilde{S}_{kk}\delta_{ij}\right) \tag{2.29}$$

the Favre-filtered rate of strain tensor

$$\tilde{S}_{ij} = \frac{1}{2}\left(\frac{\partial \tilde{u}_i}{\partial x_j} + \frac{\partial \tilde{u}_j}{\partial x_i}\right) \tag{2.30}$$

and the subgrid-scale viscous stresses

$$\tau_{ij} = \bar{\rho}\left(\widetilde{u_iu_j} - \tilde{u}_i\tilde{u}_j\right) \tag{2.31}$$

are given. The subgrid-scale heat flux (q_j^{SGS}) arise due to the filtering operator done on the convective term, i.e.

$$q_i^{SGS} = \bar{\rho}\left(\widetilde{u_ih} - \tilde{u}_i\tilde{h}\right) \tag{2.32}$$

As can be realized the terms τ_{ij} and q_i^{SGS} have to be modelled which will be explained in the following section.

2.6 Subgrid-Scale Model

Since only the resolved turbulent scales are solved for, a subgrid model is necesserary to solve for the turbulent scales which cannot be resolved by the grid and the discretization scheme. There are many SGS models, both static and dynamic ones. In dynamic models, the SGS constant, C_s is calculated for each timestep. The model used in this project, Smagorinsky is a static one with constant C_s. This model was chosen because it is the most common one, gives reliable results and is much less computational demanding compared with a dynamic one. The model is given by

$$\begin{aligned} \tau_{ij} - \frac{1}{3}\delta_{ij}\tau_{kk} &= -2\nu_{sgs}\bar{S}_{ij} \\ \nu_{sgs} = (C_s\Delta)^2\sqrt{2\bar{S}_{ij}\bar{S}_{ij}} &= (C_s\Delta)^2\left|\bar{S}\right| \\ \bar{S}_{ij} &= \frac{1}{2}\left(\frac{\partial \tilde{u}_i}{\partial x_j} + \frac{\partial \tilde{u}_j}{\partial x_j}\right) \end{aligned} \tag{2.33}$$

where C_s is the Smagorinsky constant and the filter width is taken as the local grid size

$$\Delta = \left(\Delta V_{IJK}\right)^{\frac{1}{3}} \tag{2.34}$$

The subgrid-scale heat flux term also has to be modelled where a temperature gradient approach is used, namely

$$q_j^{SGS} = C_p\frac{\mu_{sgs}}{Pr_t}\frac{\partial \tilde{h}}{\partial x_j} \tag{2.35}$$

2.7 Transport equations for species

Transport equations have to be solved for the different species, O_2, N_2 and $C_{16}H_{34}$. The index k corresponds to the different species.

$$\frac{\partial \rho Y_k}{\partial t} + \frac{\partial \rho u_i Y_k}{\partial x_i} = \frac{\partial}{\partial x_i}\left((\mu + \mu_t)\frac{\partial Y_k}{\partial x_i}\right) = \dot{\omega}_k \tag{2.36}$$

where the turbulent viscosity is defined as

$$\mu_t = \rho c_\mu \frac{k^2}{\epsilon} \tag{2.37}$$

2.8 Turbulent jet physics

When a gas jet at high velocity enters a quiescent surrounding, high shear stresses are created due to the strong velocity gradients. They produce a strong turbulent mixing of the two flows (the fuel jet with its surrounding). A cone shaped jet is formed due to the break down of the core in the inner region. Entrainment into the jet is responsible for the expansion in its cross-section. The centerline velocity decreases as the cross-section of the jet grows. The radial velocity profile in the jet region develops as a Gaussian curvature.

3 Method

OpenFOAM, which is an open source CFD Toolbox, build up on a set of C++ modules, allowing full control over the calculations. It uses a finite volume method (FVM) formulation to solve the system of partial differential equations that characterize fluid flows. In order to calculate the concentration for the different gas phases present in the domain, the solver *reactingFoam* has been selected. The solver also accounts for chemical reactions, though no chemical reactions are considered in this work. To adapt the solver for LES calculations, set-up is provided in [5]. For further information regarding the solver, see [2] and [8].

3.1 Computational mesh for the $k - \epsilon$ simulations

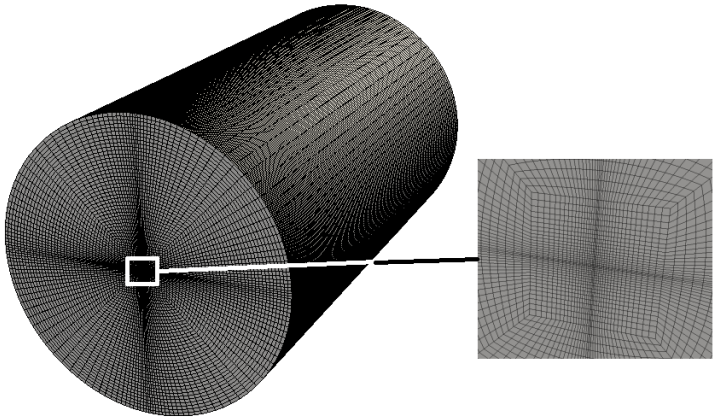

Figure 3.1: Computational mesh for the free volume domain generated in *OpenFOAM*

The overall appearance of the mesh is a cylinder where the gas is injected into the domain through the inlet which is located within the square in Figure (3.1). The inlet is located at the top of the cylinder as shown in Figure (3.1). The cut-out part is showing the inlet, i.e a squared profile with a cell resolution of 3 cells in each direction where an O-grid surrounds it. Grid refinements have been utilized to resolve the flow at the inlet. The cellsize in the inlet region is 0.0833 [mm] in both x- and y direction. There are 160 cells in the z-direction with a grading of 4 (from fine near the inlet to coarser at the bottom of the cylinder). The mesh contains approximately 1 million cells.

3.2 Boundary conditions

To validate the calculations, as mentioned earlier, an equivalent gas jet will be used in the calculations as a verification parameter. By an equivalent gas jet it is meant that the vapor penetration will have the same characteristics as vapor penetration from the evaporated liquid spray. The cell with vapor fraction of $C_{16}H_{34}$ exceeding 1 % and also has the furthest position from the injection inlet is tracked for each time step. This gas jet will be compared to experimental data presented by Siebers and Naber[10][11]. Inlet temperature and mass flow are held constant according to

$$\dot{m}_{in} = 14.1 \left[\frac{g}{s}\right] \tag{3.1}$$

$$T_{in} = 447[K] \tag{3.2}$$

Variations of the chamber and inlet pressures are taken from the experimental data where three different values are utilized, namely 18.61, 81.47 and 168 [bar]. They will be referred to as the 18-, 81- and 168 pressure cases. The specific gas constant for n-hexadecane is calculated according to

$$\bar{R}_{C_{16}H_{34}} = \frac{R}{M(C_{16}H_{34})} = \frac{8.314472 \cdot 10^3}{(16 \cdot 12 + 34 \cdot 1)} = 36.7897 \left[\frac{J}{kg \cdot K}\right] \tag{3.3}$$

where the ideal gas law gives density of n-Hexadecane

$$\rho_{in} = \frac{p_{ch}}{\bar{R}_{C_{16}H_{34}} \cdot T_{in}} = \frac{1.861 \cdot 10^6}{36.7897 \cdot 447} = 113.165 \left[\frac{kg}{m^3}\right] \tag{3.4}$$

Using the conservation of mass the inlet velocity, U_{in} is calculated. The inlet nozzle is square and to illustrate the calculation process a side of D_{in}=1.5 [mm] is used as an example below.

$$\begin{aligned} \dot{m}_{in} &= \rho_{in} U_{in} A_{in} = \rho_{in} U_{in} \left(D_{in}\right)^2 \\ \Longrightarrow U_{in} &= \frac{\dot{m}_{in}}{\rho_{in} \left(D_{in}\right)^2} = \frac{14.1 \cdot 10^{-3}}{113.165 \cdot (1.5 \cdot 10^{-3})^2} = 55.3764 \left[\frac{m}{s}\right] \end{aligned} \tag{3.5}$$

As can be seen in equation (3.4), the inlet density for each "pressure-case" will be the same and in order to fulfill the "constant inlet mass flow"-criteria, D_{in} or U_{in} are varied in equation (3.5). Since the $k-\epsilon$ model requires boundary conditions for the kinetic energy (k) and dissipation (ϵ), some simple formulas have been used for the inlet and the internal chamber cells

$$k_{in} = 0.2U_{in}^2, \qquad \epsilon_{in} = \frac{k_{in}^{3/2}}{0.2D_{in}}, \qquad k_{ch} = 0.1, \qquad \epsilon_{ch} = 0.5\frac{k_{ch}^{3/2}}{L_{min(grid)}} \tag{3.6}$$

where the $L_{min(grid)}$ is chosen to be the smallest cell side of the inlet patch. Table (3.1) presents the boundary conditions calculated according to the formulas (3.6) where side length and pressure have been varied.

Table 3.1: Boundary conditions for the different k-ϵ cases

D_{in} [mm]	Pressure [bar]	Density $[kg/m^3]$	U_{in} [m/s]	k_{in} $[m^2/s^2]$	ϵ_{in} $[m^2/s^3]$	ϵ_{ch} $[m^2/s^3]$
0.5	18	113.2	498.4	$4.97{\cdot}10^4$	$1.107{\cdot}10^{11}$	95.2
	81	495.3	113.9	2594.6	$1.32{\cdot}10^9$	95.2
	168	1021.6	55.2	609.6	$1.505{\cdot}10^8$	95.2
0.55	18	113.2	411.9	$3.4{\cdot}10^4$	$5.68{\cdot}10^{10}$	87.8
	81	495.3	94.1	1771	$6.78{\cdot}10^8$	87.8
	168	1021.6	45.6	415.9	$7.71{\cdot}10^7$	87.8
0.6	18	113.2	346.1	$2.3957{\cdot}10^4$	$3.09{\cdot}10^{10}$	79.1
	81	495.3	79.1	1250	$3.68{\cdot}10^8$	79.1
	168	1021.6	38.6	299	$4.2{\cdot}10^7$	79.1

The specie concentrations are also needed as boundary conditions, and are given in Table (3.2)

Table 3.2: Boundary conditions of specie concentration

Region	Specie concentration		
	O_2	N_2	$C_{16}H_{34}$
Inlet	0	0	1
Chamber	0.23	0.77	0

The boundary conditions at all walls, are no-slip conditons. The inlet velocity profiles in all cases are uniform, i.e. no fully developed flow is assumed.

3.3 Penetration curves using the $k-\epsilon$ model

The results of the cases given in Table (3.1) are illustrated in the following three figures.

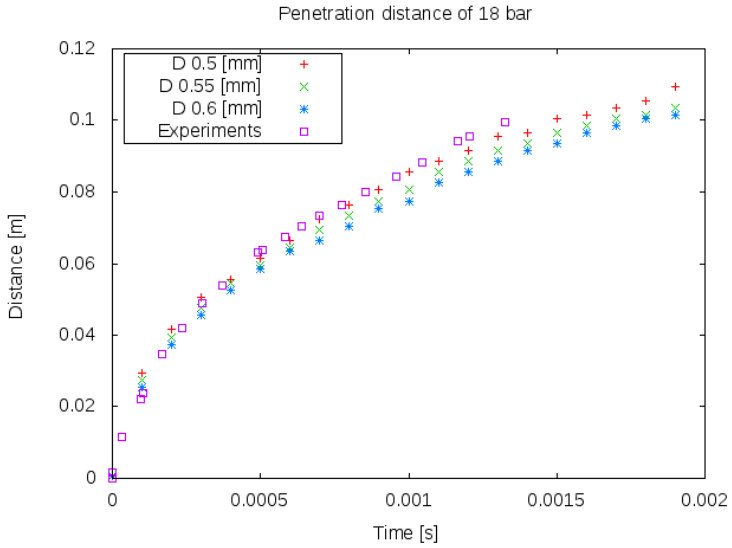

Figure 3.2: Penetration curve at 18 bar with standard k-ϵ model

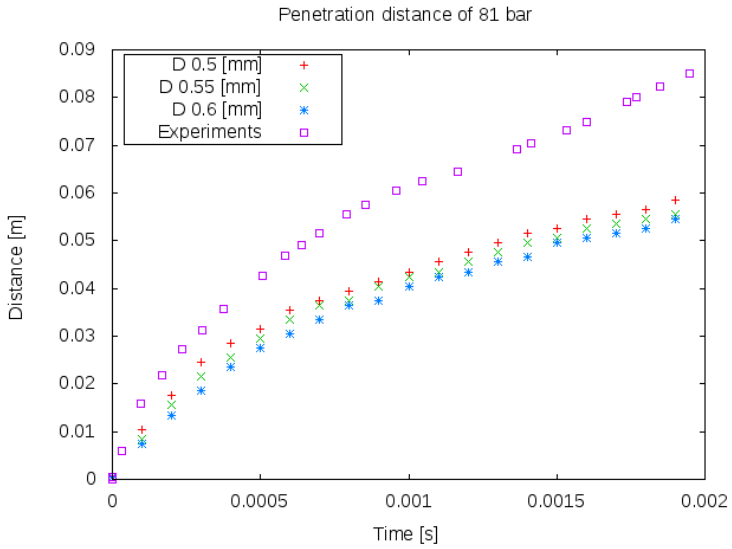

Figure 3.3: Penetration curve at 81 bar with standard k-ϵ model

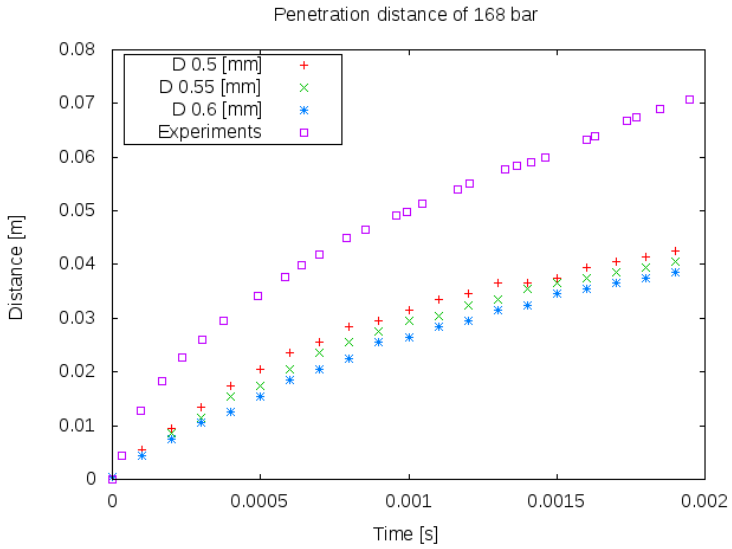

Figure 3.4: Penetration curve at 168 bar with standard k-ϵ model

The results aimed for are the comparisons that are as good as the experimental data for 18 [bar], Figure (3.2) but for all pressures. Since the 168-case is deviating strongly from the experimental data, a modification of the inlet side length and velocity are inevitable. A decrease in chamber pressure consequently leads to an increase of the penetration [9], which can be seen. Worth noting is however that the results obtained in [7] have different coefficients than those given in Table (2.1), namely the values given in Table (3.3). Standard k-ϵ model poorly predicts jet flow, therefore the tuned coefficients are used. Consequently, the first is to modify them and find out how it influences the penetration rate.

Table 3.3: Tuned constants for the k-ϵ model

$C_{\epsilon 1}$	$C_{\epsilon 2}$	$C_{\epsilon 3}$	σ_k	σ_ϵ
1.55	1.92	-0.33	1	1.58

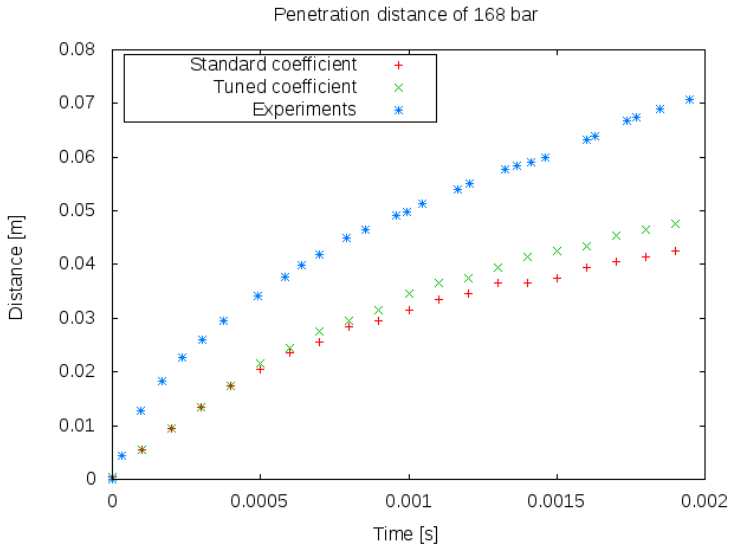

Figure 3.5: Penetration curve at 168 with standard vs tuned coefficients

As can be seen in Figure (3.5), the difference between standard and tuned coefficients are negligible up til approximately 0.5 [ms] but then the one with tuned coefficients acting more like the experiment.

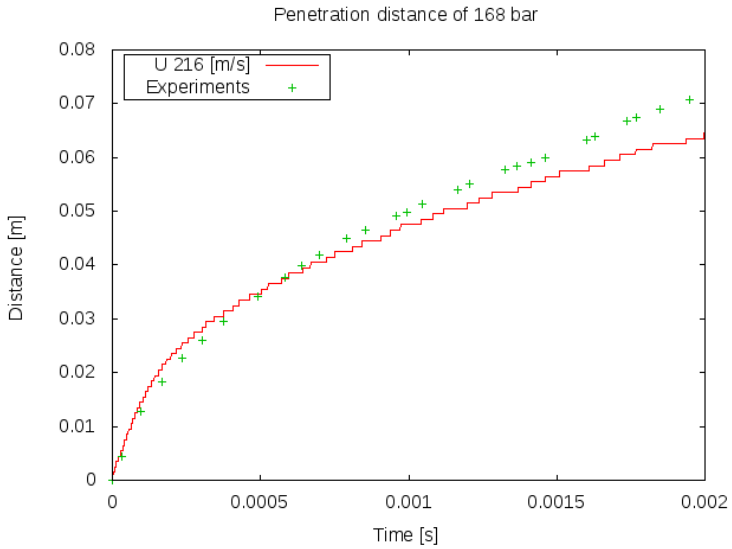

Figure 3.6: Penetration curve at 168 bar with tuned coefficients

Through an estimation, the inlet velocity can be approximated by help from the initial slope of the experimental curve. This is done in and shown in Figure (3.6). The inlet velocity was approximated as 216 [m/s] giving an inlet side length of 0.25 [mm], which seems to agree with the experimental data.

3.4 Numerical schemes for the $k-\epsilon$ simulations

.
The used schemes are provided in Table (3.4)

Table 3.4: Numerical schemes used for the k-ϵ calculations

Numerical scheme	Example	Properties	Set-up
ddtSchemes	$\partial\phi/\partial t$	All	Euler
gradSchemes	$\partial\phi/\partial x_i$	p	Gauss linear
divSchemes	$\partial u_i\phi/\partial x_i$	U,Y,h,ϵ,k	upwind
Laplacian schemes	$\partial/\partial x_i\mu_t\partial\phi/\partial x_i$	All	Gauss linear corrected

3.5 Running parameters for the $k-\epsilon$ simulations

The default convergence criteria is set to 10^{-6} and has been kept in this work. This is believed to be enough for all computations. A sensitivity study showed that a timestep of $5 \cdot 10^{-7}$ was required in order to maintain stability of the simulations.

4 Results

4.1 Computational meshes for LES

The results obtained from a simulation are obviously influenced by the quality of the computational mesh. In this work, the mesh has been constructed both by *OpenFOAM*s mesh generating utility, *blockMesh* but also created in *StarCCM+*, which is transformed into *OpenFOAM*s mesh format. Common geometry parameters for both types of meshes are given in Table (4.1).

Table 4.1: Common geometry parameters for both meshes

D_{in}	0.25 mm
R_{cyl}	30 mm
H_{cyl}	110 mm
Celltype	hexahedrons

Explanation of the abbreviation used: D_{in}, R_{cyl} and H_{cyl} are the jet inlet side length, radius, and height of the cylinder/box. $L_{box} = 2R_{cyl}$ corresponds to the length of one side of the box created in *StarCCM+*.

4.1.1 OpenFOAM generated meshes

A couple of illustrations of the computational domain will follow.

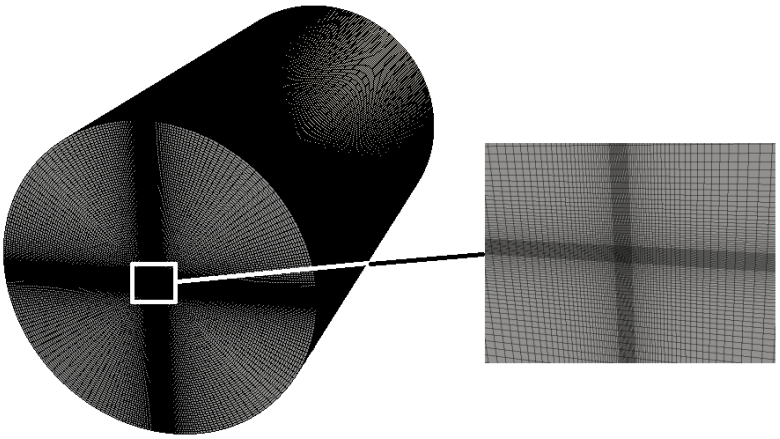

Figure 4.1: Computational mesh for the free volume domain generated in *OpenFOAM*

The overall appearance of the mesh is a cylinder where the gas is injected into the domain through the inlet which is located within the square in Figure (4.1). The inlet is located at the top of the cylinder as shown in Figure (4.1). The cut-out part is showing the inlet, i.e a squared profile with a cell resolution of 20 cells in each direction where an O-grid surrounds it. Grid refinements have been utilized to resolve the flow at the inlet. The

cellsize in the inlet region is 0.0125 [mm] in both x- and y direction. There are 270 cells in the z-direction with a grading of 12 (from fine near the inlet to coarser at the bottom of the cylinder).

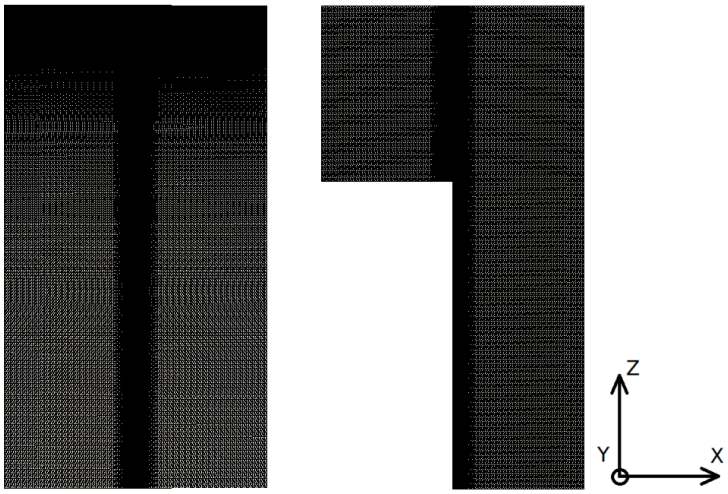

Figure 4.2: Cross-section of the meshes showing the domain generated in *OpenFOAM*

Two computational meshes generated by *OpenFOAM* have been used which can be illustrated in Figure (4.2). Three different geometries are considered. The reason why the third geometry is not generated by help from *blockMesh*, are the difficulties generating the curved geometry with good quality. The obstacle, a flat plate, is positioned at height 70 [mm]. The number of cells are 8.75 and 6 million, respectively.

4.1.2 StarCCM+ generated meshes

The procedure of constructing the meshes entirely by *blockMesh*, specifying vertices, blocks and gradings of the cells, can be very tricky and time consuming. One way around this problem is to preprocess elsewhere, i.e. construct the mesh in another program and then convert it to *OpenFOAM* format. The mesh generation tool in *StarCCM+* was used for preprocessing.

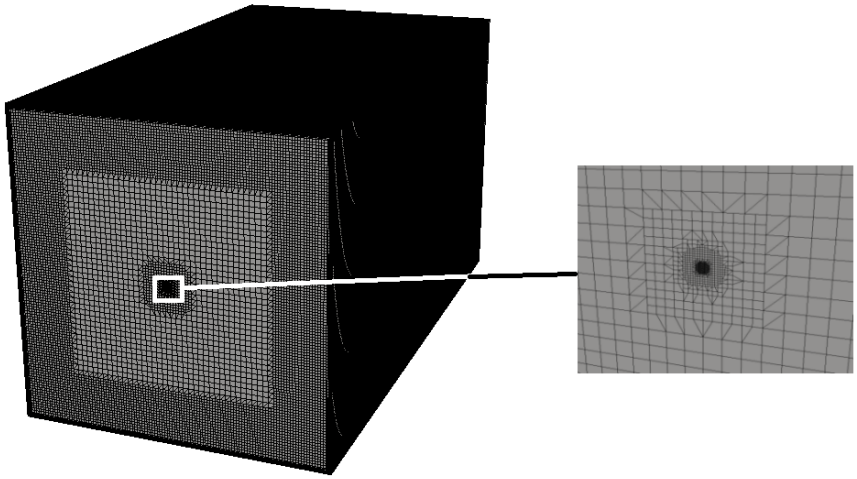

Figure 4.3: Computational domain for the free volume generated in *StarCCM+*

In Figure (4.3), the top of the domain is shown with a detailed enlargement of the inlet. A big difference between the meshes presented in the former section and the meshes generated by *StarCCM+* are the shapes, the latter are squared in shape. The cut-out part is showing the inlet, i.e a squared profile with a cell resolution of 16 cells. That gives a cellsize of 0.015625 [mm] at the inlet.

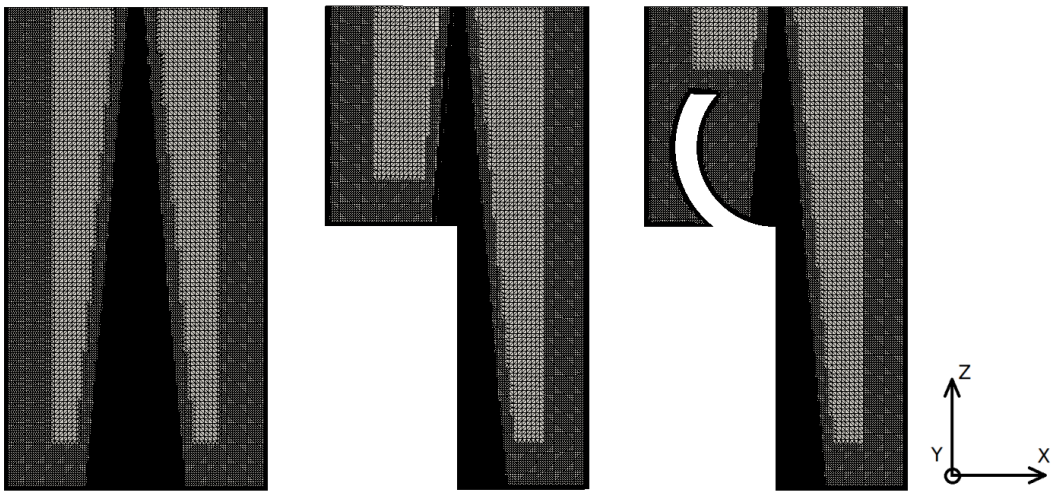

Figure 4.4: Computational domains generated in *StarCCM+*

As can been seen in Figure (4.4), the interior structure of the meshes looks different compared to Figure (4.2). A coned-like refinement has been made along the assumed jet path in order to better resolve the velocity gradients within the jet and hence the generated turbulence. The boundary layers are refined in all meshes along the walls, flat plate and the curved plate. The number of cells are approximately 10, 7 and 6 million, respectively.

4.2 Numerical schemes for LES

OpenFOAM provides a large number of choices for the user when it comes to numerical schemes settings. The used schemes are provided in Table (4.2).

Table 4.2: Numerical schemes used for the LES calculations

Numerical scheme	Example	Properties	Set-up
ddtSchemes	$\partial\phi/\partial t$	All	backward
gradSchemes	$\partial\phi/\partial x_i$	p	Gauss linear
divSchemes	$\partial u_i\phi/\partial x_i$	U	Gauss limitedLinearV 1
divSchemes	$\partial u_i\phi/\partial x_i$	k,p	Gauss limitedLinear 1
divSchemes	$\partial u_i\phi/\partial x_i$	Y,h	upwind
Laplacian schemes	$\partial/\partial x_i\mu_t\partial\phi/\partial x_i$	All	Gauss linear corrected

It was necessary to choose a second order scheme for the time derivatives aswell as other properties to receive a stable LES calculation. Further information regarding the various settings provided by *OpenFOAM*, can be found at [1].

4.3 Running parameters for LES

The default convergence criteria is set to 10^{-6} and has been kept in this work. This is believed to be enough for all computations. A sensitivity study showed that a timestep of 10^{-8} was required in order to maintain stability of the simulations.

4.4 Free volume domain

Based on the inlet side length D_{in}, the Reynolds number is approximately 2.4 million telling that the flow is fully turbulent. We can therefore expect turbulent structures in the gas jet penetrating the domain. The penetration curves for the *OpenFOAM* and *StarCCM+* generated meshes are given in Figure (4.5) and will for now be referred to as the *OF* and *CCM* meshes. In the following the results of the LES simulations are discussed.

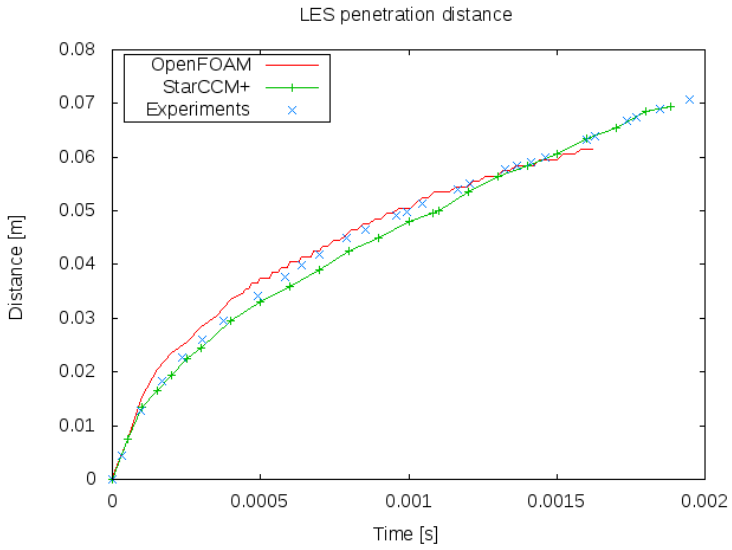

Figure 4.5: LES penetration curve of free volume for both meshes

Both results agree well with the experimental data. As can be seen, the gas jet is slightly overpredicted for the *OF*-mesh. This is believed to be a result of the much coarser mesh

in the spray core which cannot fully resolve the turbulence. n-Hexadecane is entering the free volume with a uniform velocity profile. However, since the turbulence causing the fluctations and mixing are not there from the beginning, the grid has to be fine enough near the nozzle to resolve the steep velocity gradients. Due to large sensitivity of the simulation, the timesteps selected turned out to impact the penetration curves. When chosing a timestep of 10^{-7}, the maximum Courant number was below 0.1 but the turbulence was not resolved and therefore, the gas did not expand due to entrainment but it have a linear behavior throughout the domain. Figure (4.6)-(4.9) present a comparison at four different timesteps after start of injection between the OF and the CCM meshes of the jet entering the domain.

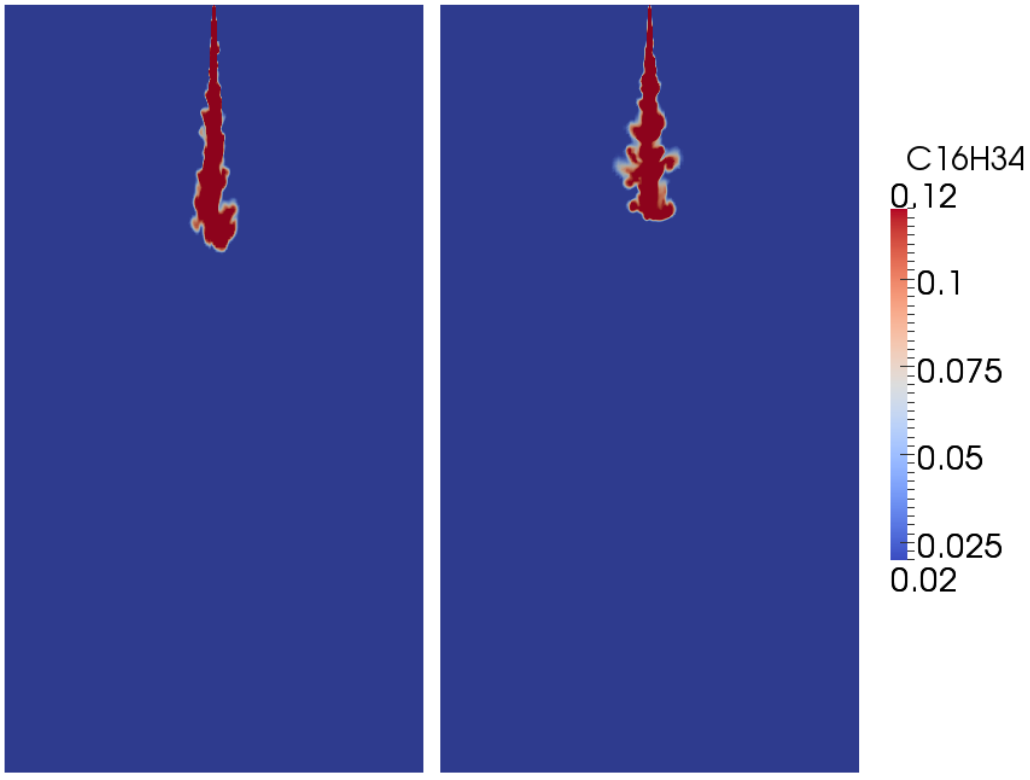

Figure 4.6: At 0.5 [ms], left: OF , right: CCM

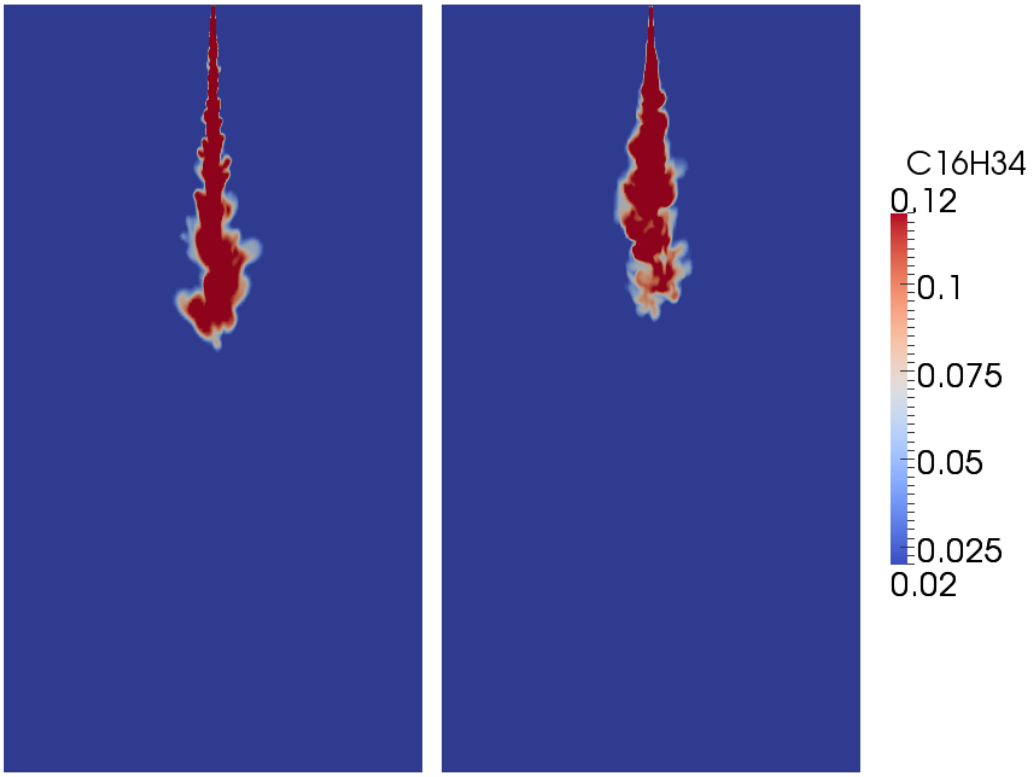

Figure 4.7: At 1 [ms], left: OF , right: CCM

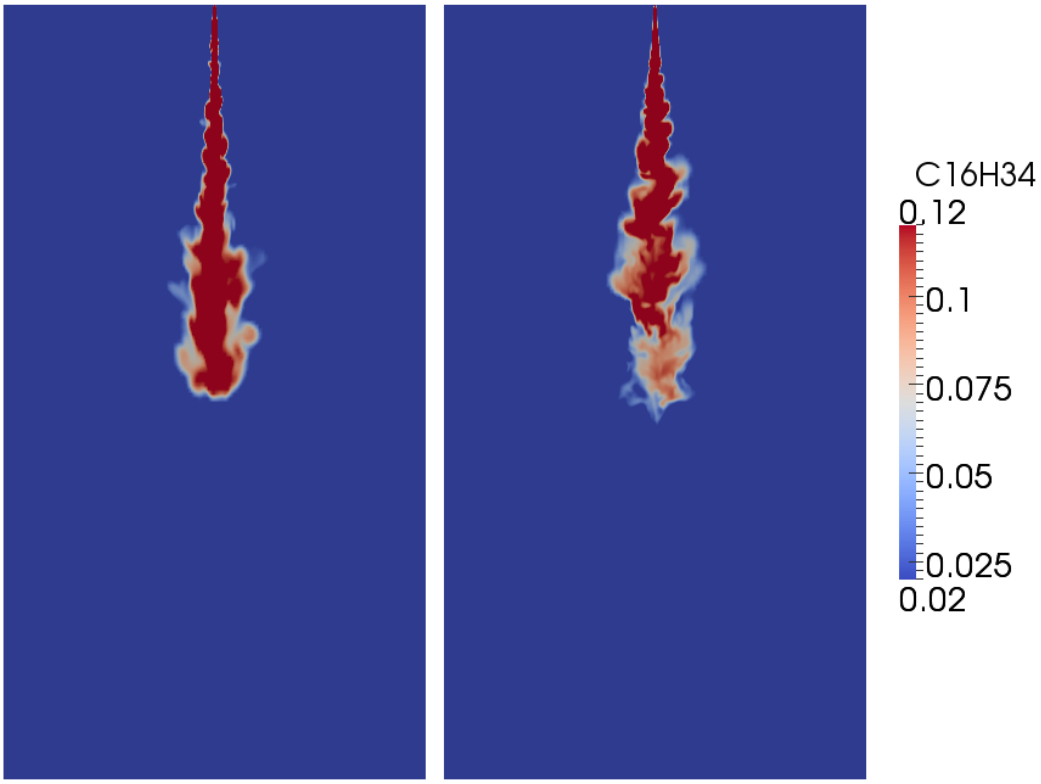

Figure 4.8: At 1.5 [ms], left: OF , right: CCM

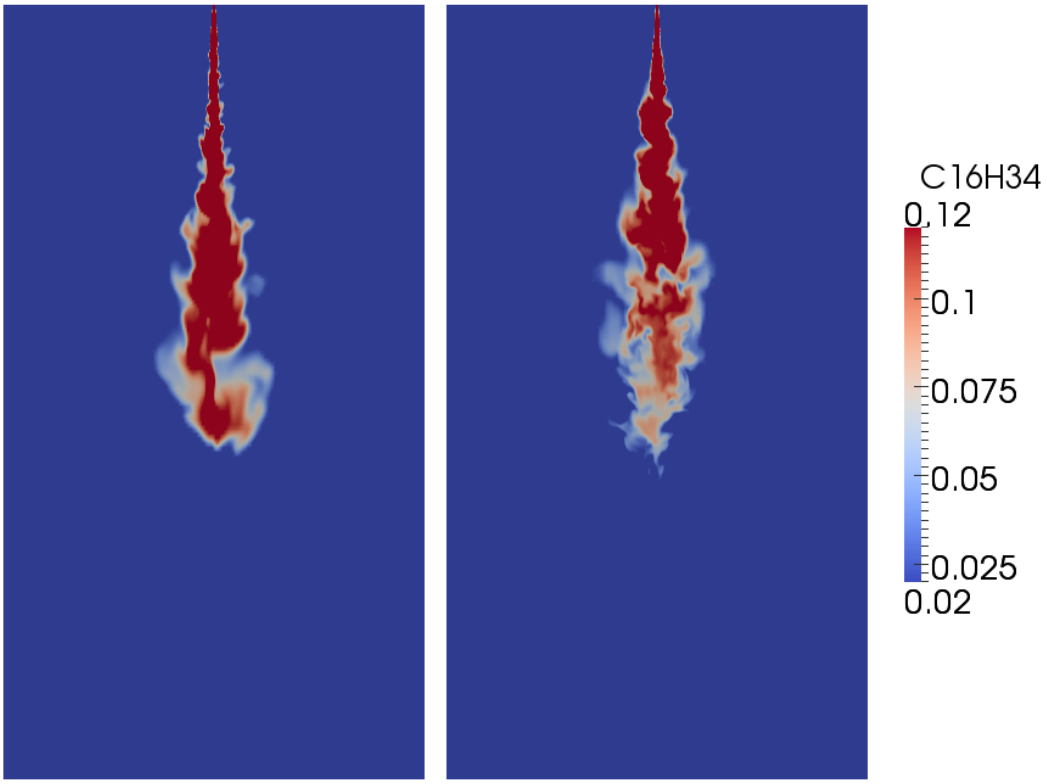

Figure 4.9: At 1.85 [ms], left: OF , right: CCM

The figures show contours of the fuel fraction between 0.02 - 0.12 reaching from lean to rich mixture where most of the combustion takes place. The stoichiometric value is considered to be 6%. According to Figure (4.5), the mesh generated in $StarCCM+$ seems to mimic the experimental data better given the penetration curve but also the spreading in the radial direction. To the left in Figure (4.9), a sharp edge surrounds the jet while it has a diffused contour in CCM. This indicates that the mixing behind the leading edge in the CCM case have proceeded much further than in the OF case. This will most likely have an effect on the combustion process. Despite this, the CCM mesh will prove not to meet our requirements as discussed in the next paragraph.

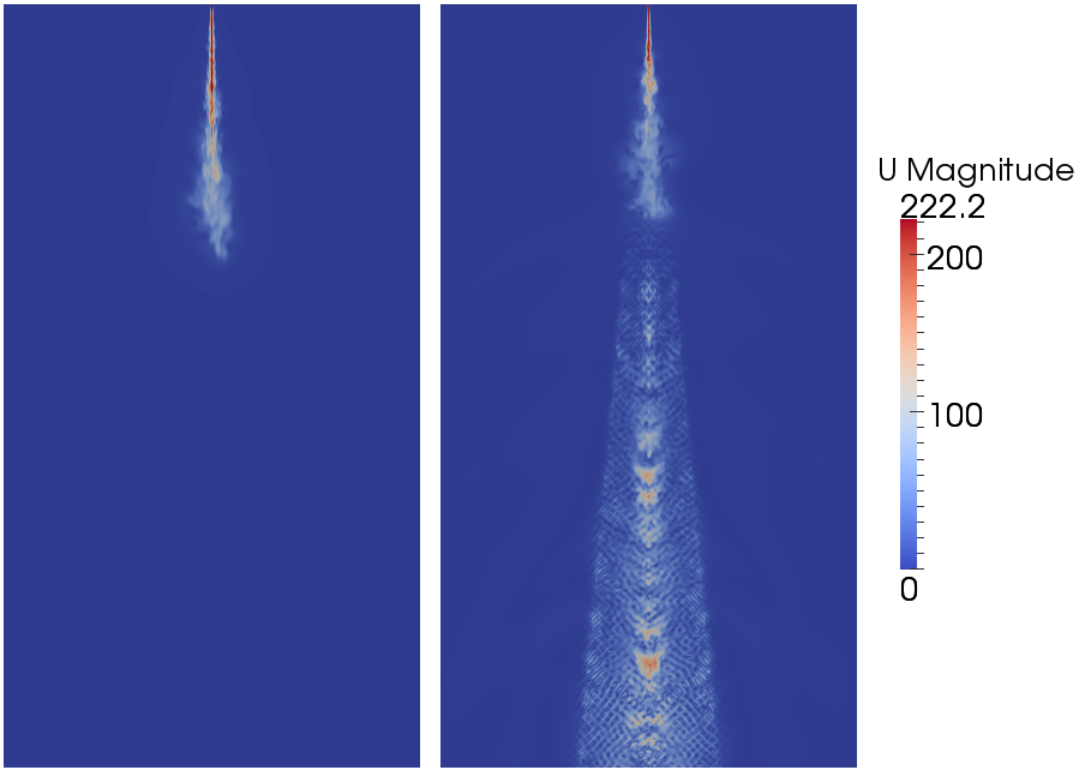

Figure 4.10: Velocity at 0.5 [ms], OF mesh to the left

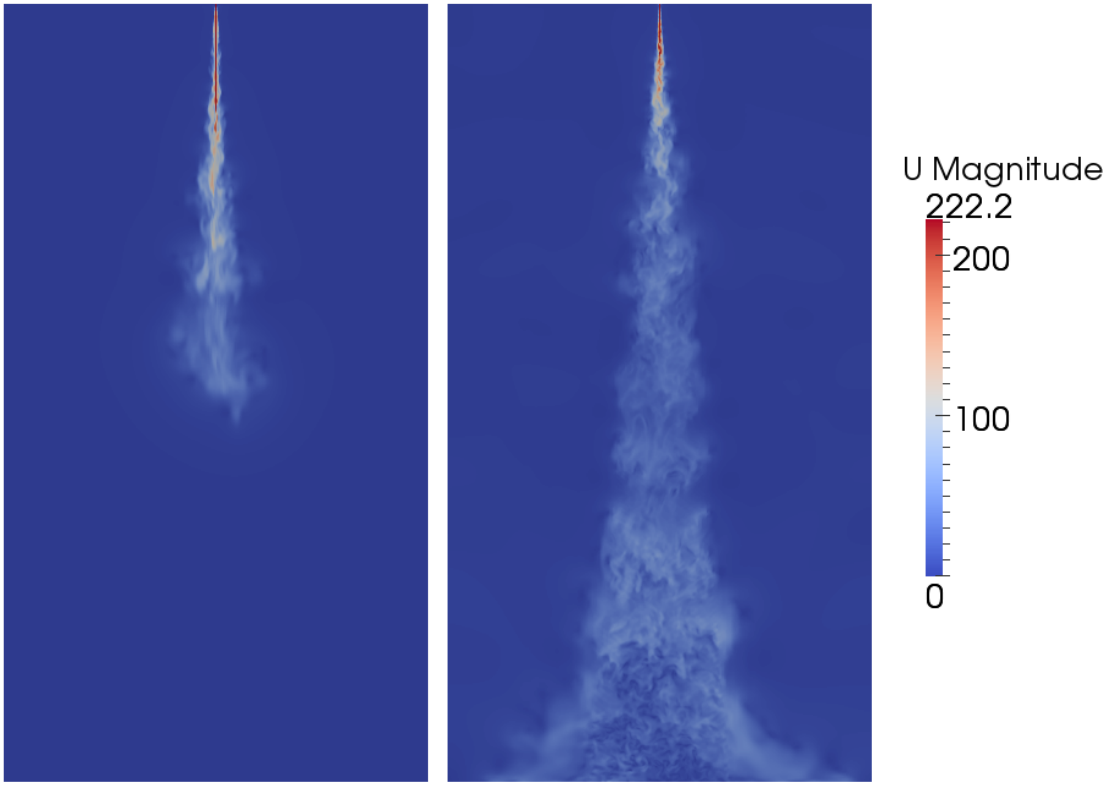

Figure 4.11: Velocity at 1.5 [ms], OF mesh to the left

A strange velocity field has somehow been generated in the lower part of the domain for

the CCM mesh, Figure (4.10) and Figure (4.11) respectively. One likely cause of this could be the mesh converter from $StarCCM+$ into $OpenFOAM$ format [6], which is known to create bad cells. The velocity field follows the mesh refinement seen in Figure (4.4). The magnitude reaches more than 100 [m/s] downstream of the jet tip position and can not be ignored. Further improvement of the mesh is necessary to continue using the CCM mesh. In the continuation, the free volume domain will therefore be the one created in $OpenFOAM$.

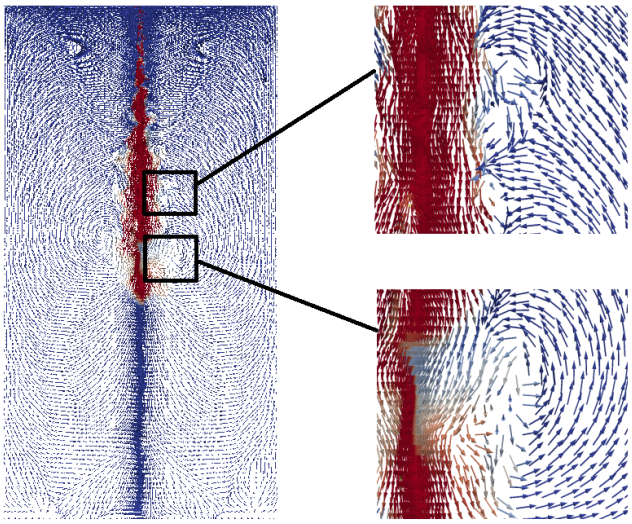

Figure 4.12: Vortices present near jet in the OF mesh

In Figure (4.12) one can see the large-scale motion generated at the jet boundaries. Ring vortices are formed, that carries the surrounding flow into the jet, hence increasing the entrainment rate. This causes the mixing of the flows and as a result, the large-scale structures are broken down, in turn, generating the small-scale turbulent mixing. Since the underlying idea is to capture the instantaneous mixing process, a comparison between the results from RANS and LES simulation will be given in the following section.

4.4.1 RANS vs LES

In Figure (4.13) a comparison of the jet penetration between the two models shows a similar behavior. One of the objectives of this work was to understand the major differencies between a RANS and a LES simulation.

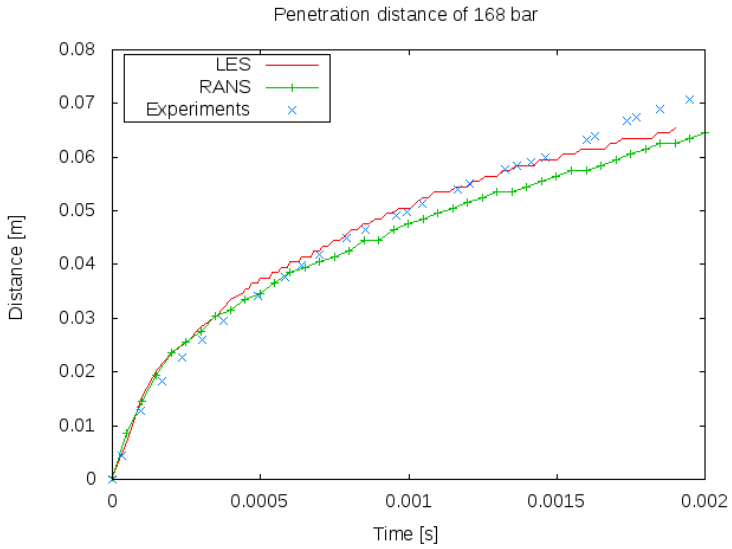

Figure 4.13: RANS, LES and experimental data for the penetration process

Not surprisingly, both the penetration curves share the same characteristics and agree well with experimental data. The main difference is however the overall appearance in regard to the instantaneous vortices captured in LES but averaged out in RANS. The mean flows are similar in both cases. All eddies larger than the cellsize are resolved in LES, but in RANS all the scales are modeled. Using LES in turbulent diesel jets is therefore of great interest since it gives insight in the mixing process of the flows. Figure (4.14) shows the isocontour of 6% $C_{16}H_{34}$ and coloured by the kinetic energy, k.

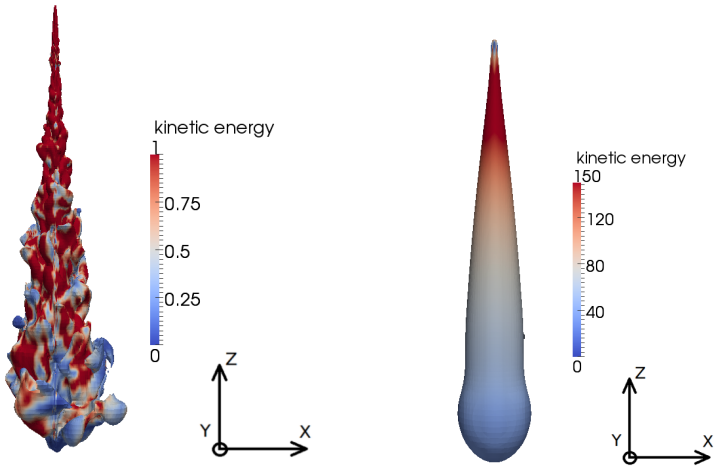

(a) LES (b) RANS

Figure 4.14: Comparison of the isosurfaces for LES and k-ϵ simulation

The turbulent kinetic energy in RANS is 150 times higher than in LES. The kinetic energy in RANS is the energy for all scales, but in LES it is the energy for the sub-grid scales, k_{SGS}. These ranges have been chosen to be able to visualize the energy as it varies on the isosurfaces.

4.5 Flat plate domain

Simulations performed on the free volume were mainly used to validate the settings, like for instance the initial conditions. Since the penetration rate is validated and turbulent vortices are captured correctly, its setup can thus be assumed to be valid. As for the free volume domain, calculations were performed on two different computational meshes for the flat plate. However, in the free volume CCM mesh, obtaining reliable results were difficult, hence this mesh was abandoned. For now on, the mesh used in the setup is the one generated in $OpenFOAM$. A flat plate is mounted 40 [mm] downstream the inlet, see Figure (4.15). This will divide the gas jet into two parts, one part follows the vertical wall and one the horizontal wall. Boundary layers will form both along the vertical and horizontal walls. The flow field in the stagnation zone has no large scale structures. This is due to the strong pressure gradient normal to the horizontal wall which keeps the boundary layer thin. The series of images, Figure (4.15), shows the development. The jet is illustrated by the stoichiometric surface. The cut-out part is showing the inlet, i.e a squared profile with a cell resolution of 20 cells.

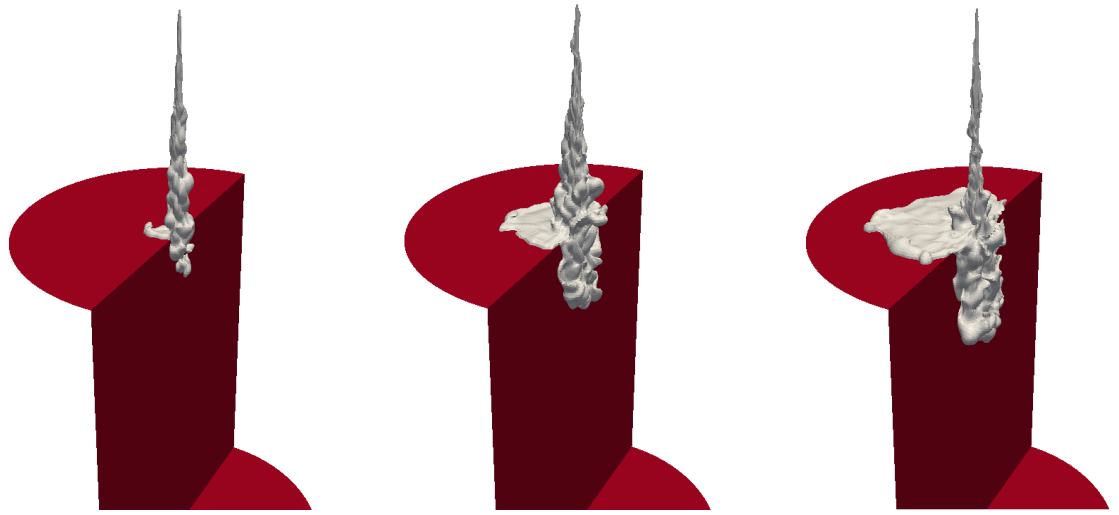

(a) 0.5 ms (b) 1 ms (c) 1.5 ms

(d) 2.0 ms (e) 2.5 ms (f) 3.0 ms

Figure 4.15: Gas jet dispersion during simulation

As the impinging jet approaches the plate, it will decelerate in the axial direction and accelerated in the radial direction simultaneously. In the stagnation zone, a pressure gradient predominates the flow and suppresses the large scale structures. The situation along the vertical wall in the direction of the gas jet is of opposite character. Here the turbulence is enhanced by the vertical wall.

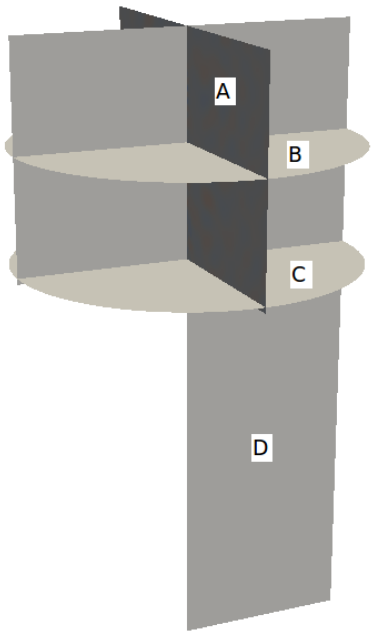

Figure 4.16: Cut planes in the flat plate domain

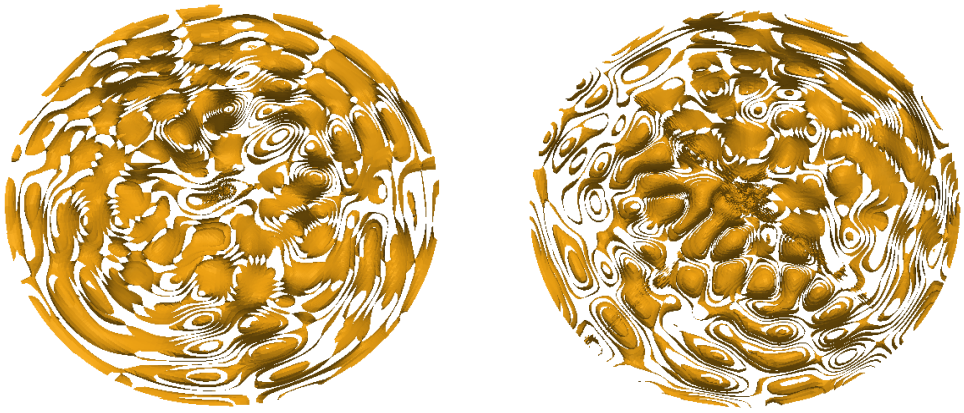

(a) Pressure at plane B, 20 mm from inlet (b) Pressure at plane C, at the flat plate

Figure 4.17: Contour plot of pressure in the domain at different heights

Before the jet hits the plate, Figure (17(a)), wave-like pressure patterns appear and spreads throughout the domain. As the jet hits the plate, Figure (17(b)), these waves break up and pressure fluctuations will have a broad spectrum due to the nature of the high Reynolds

number jet. Further insight and knowledge around this area are therefore of interest. An impinging jet, is a collection of flow situations, free turbulent jet, creation of strong vortices along the shear layer and stagnation zone, each of these are scientific research areas on their own. Because of the high complexity, much more simulations are needed to provide a basic knowledge.

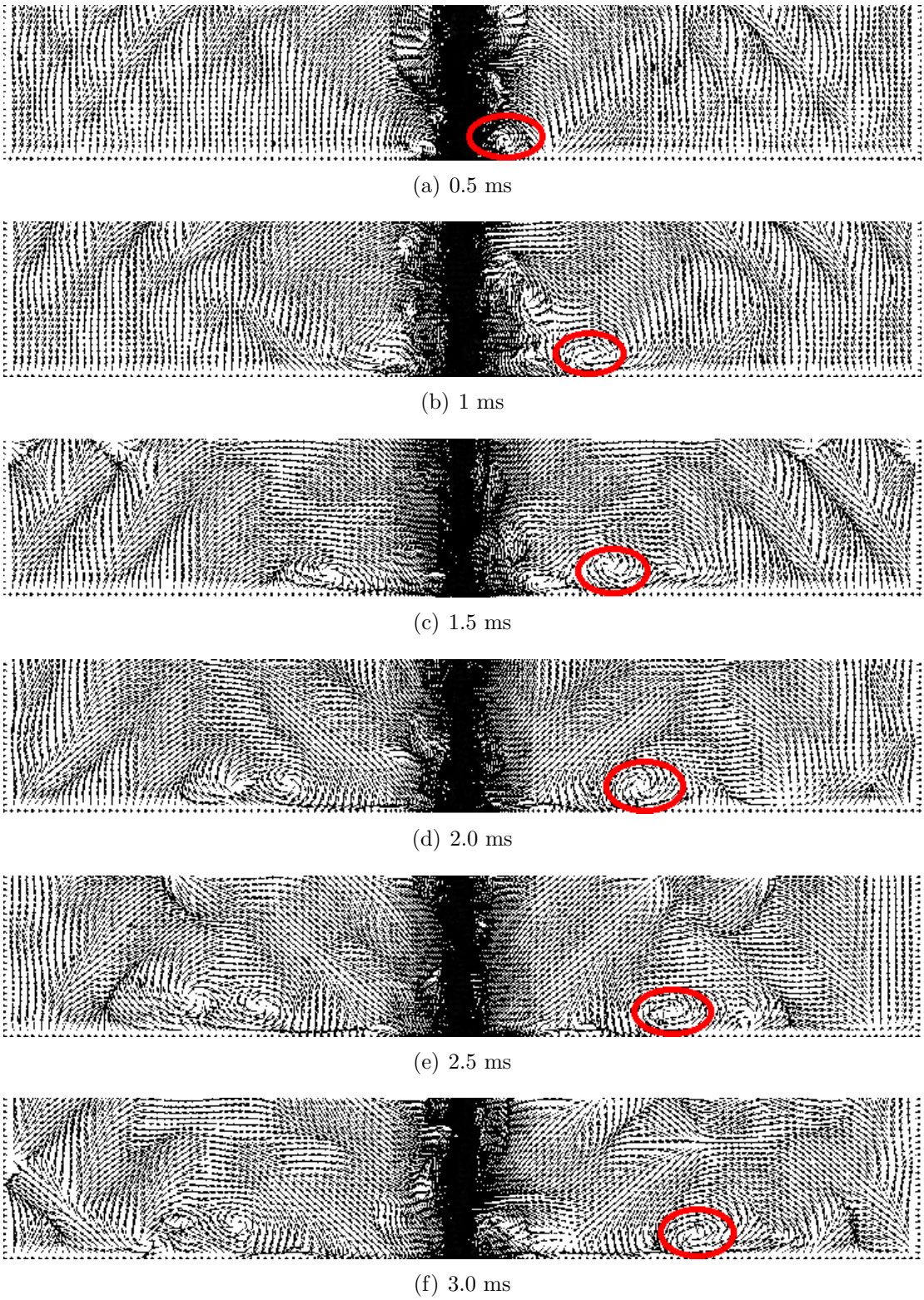

(a) 0.5 ms

(b) 1 ms

(c) 1.5 ms

(d) 2.0 ms

(e) 2.5 ms

(f) 3.0 ms

Figure 4.18: Vectors of velocity where eddies expand along the impinging surface

Figure (4.18) shows the horizontal plate, seen in plane A in Figure (4.16), where small eddies arise near the jet core and travels in the radial direction while they grow in size. It is important to note that the vectors are all equal in size to illustrate the direction of the velocity and not its magnitude.

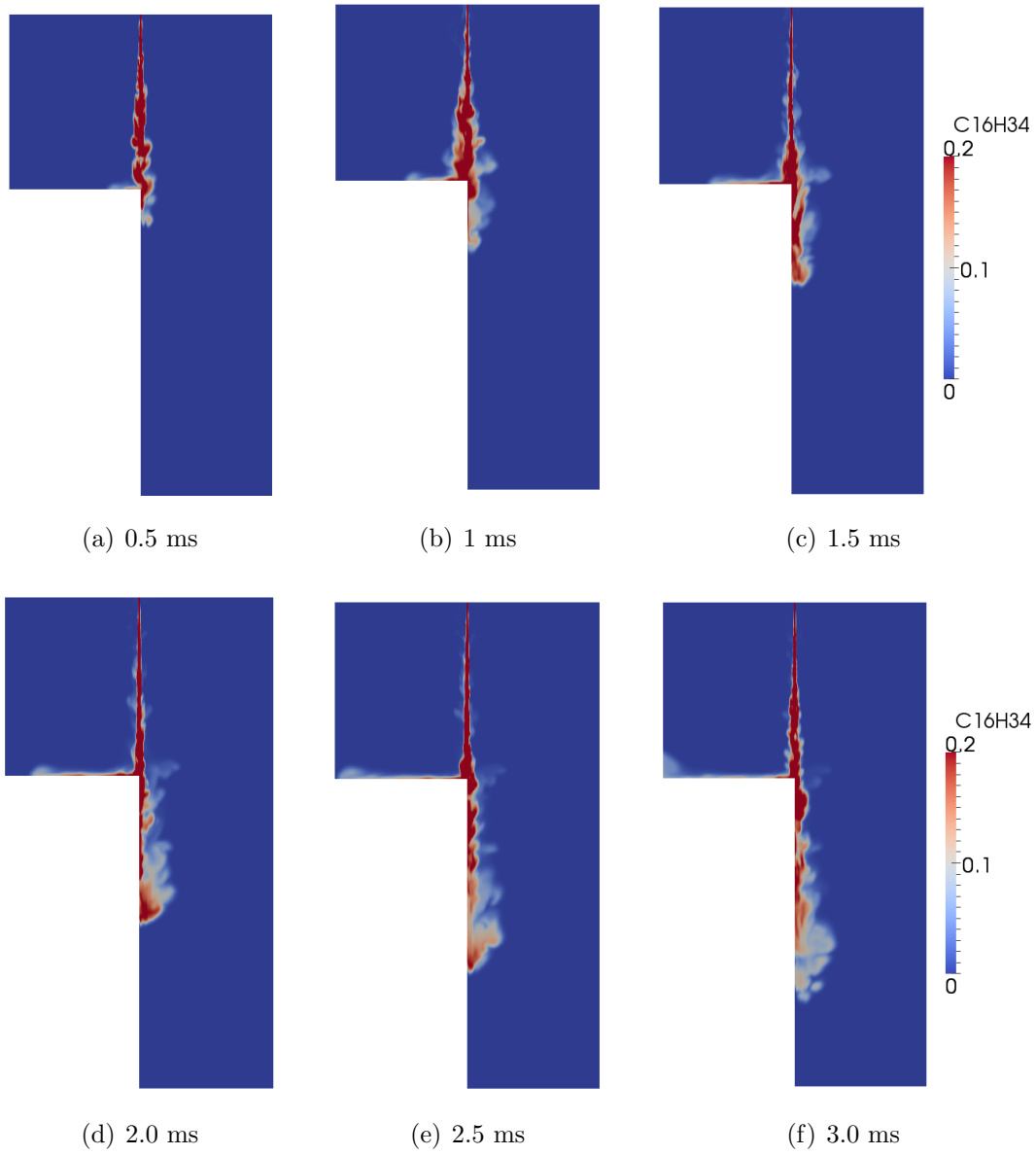

(a) 0.5 ms (b) 1 ms (c) 1.5 ms

(d) 2.0 ms (e) 2.5 ms (f) 3.0 ms

Figure 4.19: Concentration of $C_{16}H_{34}$ in range of 0-0.2

The regions colored in red in Figure (4.19) illustrate where the interesting combustion processe take place. The stoichiometric value is within this range at a value of 0.06. How the gas jet is spreading along the vertical and horizontal wall depends strongly on the mesh quality. The mesh resolution normal to the horizontal plate is poor and therefore the turbulence cannot be resolved correctly. A way to go around this is to use wall functions to estimate the velocity profile, but this has been reported not to be a well established concept dealing with impinging jets [3]. Along the vertical wall, the resolution is far better than the horizontal. The transition from a liquid phase into a gas phase forces the substance to expand in the radial direction. The gas expansion is also due to the combustion after the phase shift. For that reason, the jet hitting the obstacle, is broader than our equivalent gas jet.

4.6 Curved wall domain

The two meshes generated in *StarCCM+* presented in previous sections were rejected due to strange behavior in the solution. However, the curved wall mesh will be too time consuming to create using the *blockMesh* utility in *OF* and hence a *CCM* mesh was required although the results can be questionable. Despite this, the results can be of interest. The curved wall is positioned 50 [mm] downstream the inlet. Cut planes in the following Figure (4.20) are used to clarify the gas motion. The cut-out part is showing the inlet, i.e a squared profile with a cell resolution of 16 cells.

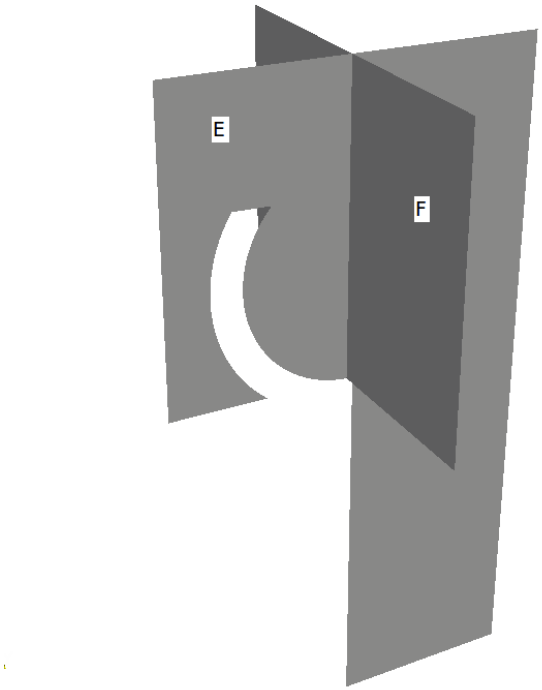

Figure 4.20: Cut planes position for further investigation

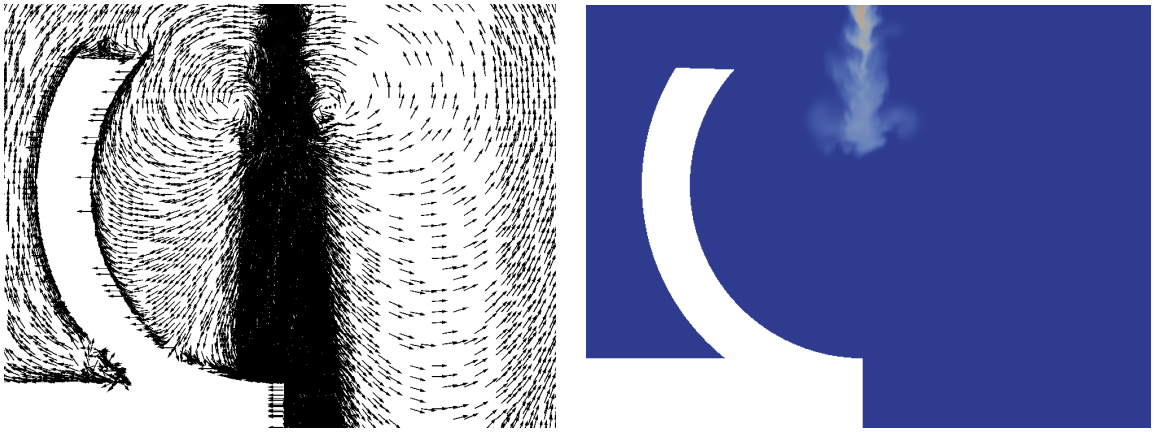

(a) 0.5 ms, at plane E

(b) 0.5 ms, at plane E

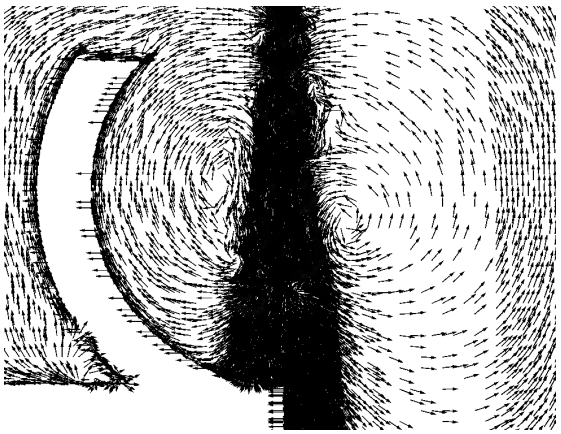

(c) 1 ms, at plane E

(d) 1 ms, at plane E

Figure 4.21: Vectors of the velocity to the left for time 0.5 and 1.0 [ms], respectively. The right figures show the gas penetrating the domain.

Despite the fact that the gas jet has not reached far into the domain (shown in Figures (21(b)) and (21(d))) large rotational structures has become visible. As before, the vectors are all equal in size to illustrate the direction of the velocity and not its magnitude. The structures, moving further downwards, into the curved wall region is enhanced compared to the structures on the free side.

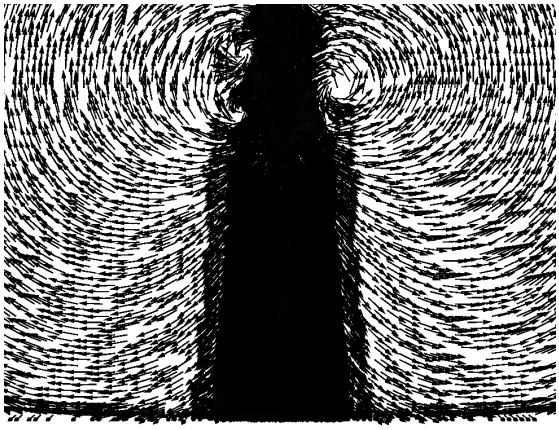

(a) 0.5 ms, at plane F

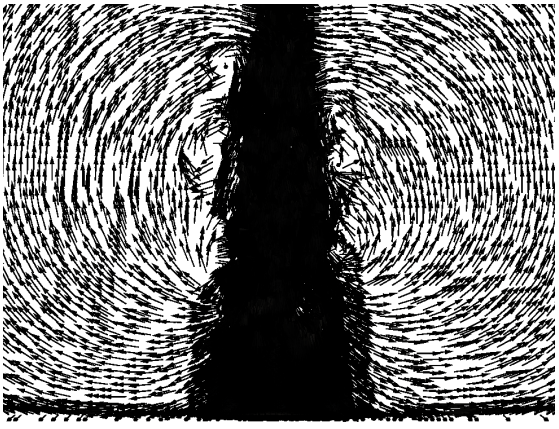

(b) 1 ms, at plane F

Figure 4.22: Vectors of the velocity for time 0.5 and 1.0 [ms], respectively

The large rotational structures can also be seen in plane F (penetration of the jet as far downstream as for Figure (4.21)). A three dimensional shaped pattern has been created. The only thing that can be concluded is that the curved wall seems to trap the vortex.

5 Conclusions

Since *OpenFOAM* does not have any particularly good mesh generator, a way to go around this is to import a mesh created in a more user-friendly software. The mesh was imported from *StarCCM+* with expectations that the mesh would not be distorted in any sence. It did however, fail to be converted flawlessly. This had been reported before, but only for much more complex geometries than the flat plate and the curved wall [6].

When LES is used for simulating turbulent jets, it is very important that the inlet region consists of sufficient number of cells to be able to resolve the flow in the shear layer regions. Otherwise it can not resolve the turbulence which in turn leads to poor agreement with characteristics of a turbulent jet. This was verified when comparing the free-volume-meshes. In a sense, both the OF and the CCM meshes can be rejected, since none of them are fulfilling the requirements of a good mesh. Also, the poor resolution at the interacting wall on the flat plate mesh is of great importance. The y^+ value was far beyond the recommended value of unity, which tells us that the flow has not been fully resolved. Since we are using a cut off filter depending on cell size, a uniform mesh would be favorable, but since number of cells would be too large compromising is inevitable.

The numerical settings have once more proven to be very important. To save time, large timesteps will be preferable. However, as a consequence, the solution gets instable due to the Courant number criteria which is supposed to be smaller than unity. It also affects the turbulence itself. If the timestep, Δt is larger than the small scale turbulent timescale t_{small} it can not be resolved which was experienced obtaining the penetration curves for all cases, particular the LES calculations.

The expectation of finding turbulent phenomenas arising due to a penetrating gas jet, can be said to be found. However its credibility can be questioned. None of our findings have been verified more than once, or in some sence twice. The irregular, random and chaotic characteristics of a gas jet have been captured which was the purpose of this work. It is unfeasible to draw any conclusions about combustion and its complexibility, considering these too simplified flow situations. In order to at least find some common features, the flow field has to be well established.

The $k - \epsilon$ model gives an averaged flow field. In most applications this model is sufficient, but it does not give much information about the instantaneous details of the flow. However, LES offers a snapshot of an instant situation which gives an insight and new understanding of the local turbulent mixing processes. Turbulence generates areas with the required concentration which is necessary for combustion.

6 Recommendations

An inject rate profile over time would be interesting to investigate. Since injection of the fuel simulated, instantaneously enters the domain and does not wear off, no end of injection (EOI) is taken into account, i.e. it is time independent. However, it could be important to see how the turbulence declines due to dissipation rates after EOI. The injection duration could also be of interest to vary.

Compare and verify if there is any difference in the development of the jet if the inlet geometry is changed to circular instead of a quadratic one. It could change the appearence and distribution of the jet in the $x - y$ plane.

Change the velocity profile from a uniform to a fully developed turbulent profile. The flow could be more accurate with a turbulent profile since it resembles a fully developed flow. This could also be generated with a pipe added to the inlet that assures fully developed flow when entering the domain.

The curvature wall and the flat wall could be simulated with different distances from the inlet to see how it affects the turbulence after impinging the obstacles.

Carry out many calculations with variation of velocity profiles, injection angles and different boundary conditions and then take an average to be able to look at production and dissipation terms for instance when doing LES.

Gradually increase the complexity of the simulations like for instance a twophase system with a liquid phase entering the domain and then evaporates.

References

[1] Openfoam user guide. http://www.openfoam.com/docs/user/, 2011.

[2] Christian Andersen and Niels E. L. Nielsen. Numerical investigations of a bfr using openfoam. http://www.projekter.aau.dk, 2008.

[3] R.S. Danielle, Jian Su Guerra, and Freire Silva. The near wall behavior of an impinging jet. *International Journal of Heat and Mass Transfer 48 (2005) 2829-2840*, 2005.

[4] J. Eismark, A. Karlsson, R. Lindgren, A. Magnusson, R. Ochoterena, and I. Denbratt. Role of formation and transportation of hydroxyl radicals for enhanced late soot oxidation in a low emissions heavy-duty diesel engine. *THEISEL 2010 Conference on Thermo- and Fluid Dynamic Processes in Diesel Engines*, 2010.

[5] Piero Iudiciani. A modified version of the reactingfoam tutorial for les. http://www.tfd.chalmers.se/~hani/kurser/OS_CFD_2009/IudicianiPeerReviewedFinalTutorial.pdf, 2010.

[6] Alexander Ivchenko. Incorporation of openfoam software into computational fluid dynamics process in volvo technology. *Tura ER-530567*, 2011.

[7] A. Kösters and A. Karlsson. A comprehensive numerical study of diesel fuel spray formation with openfoam. *2011 SAE International*, 2011.

[8] Andreas Lundstrom. reactingfoam. http://www.tfd.chalmers.se/~hani/kurser/OS_CFD_2007/AndreasLundstrom/reactingFoam.pdf, 2007.

[9] Lionel Martinez, Adlène Benkenida, and Bénédicte Cuenot. A study of the diesel spray dynamics using eulerian-eulerian large eddy simulation. *International Journal of Multiphase Flow*, 2011.

[10] J.D. Naber and D.L. Siebers. Effects of gas density and vaporization on penetration and dispesion of diesel spray. *SAE paper 960034*, 1996.

[11] D.L. Siebers. Liguid-phase fuel penetration in diesel sprays. *SAE paper 980809*, 1998.